

Three-dimensional single-mode nonlinear ablative Rayleigh-Taylor instability

R. Yan, R. Betti, J. Sanz, H. Aluie, B. Liu, and A. Frank

Citation: *Physics of Plasmas* **23**, 022701 (2016); doi: 10.1063/1.4940917

View online: <http://dx.doi.org/10.1063/1.4940917>

View Table of Contents: <http://scitation.aip.org/content/aip/journal/pop/23/2?ver=pdfcov>

Published by the [AIP Publishing](#)

Articles you may be interested in

[The late-time dynamics of the single-mode Rayleigh-Taylor instability](#)

Phys. Fluids **24**, 074107 (2012); 10.1063/1.4733396

[Combined effect of viscosity and vorticity on single mode Rayleigh–Taylor instability bubble growth](#)

Phys. Plasmas **18**, 022109 (2011); 10.1063/1.3555523

[Experimental study of the single-mode three-dimensional Rayleigh-Taylor instability](#)

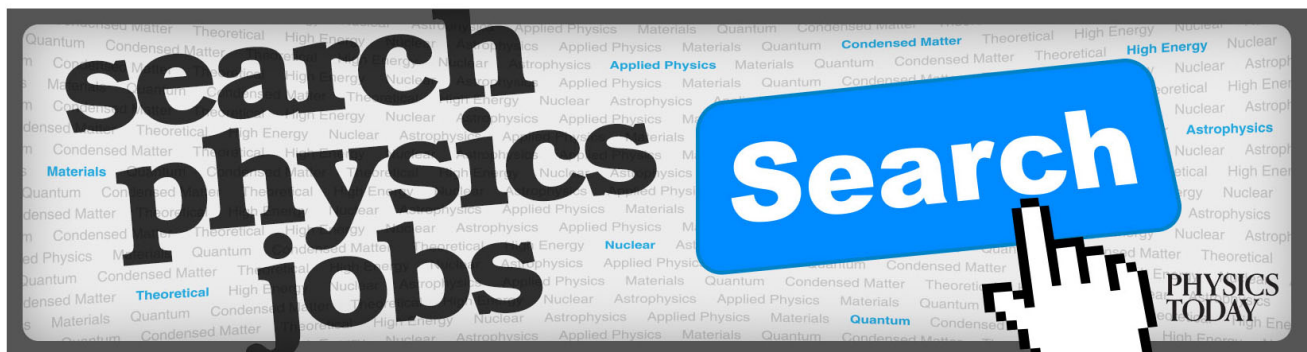
Phys. Fluids **19**, 124102 (2007); 10.1063/1.2813548

[Mixing induced by Rayleigh–Taylor instability in a vortex](#)

Phys. Fluids **17**, 021703 (2005); 10.1063/1.1852580

[Three-dimensional bubbles in Rayleigh–Taylor instability](#)

Phys. Fluids **11**, 3306 (1999); 10.1063/1.870189



Three-dimensional single-mode nonlinear ablative Rayleigh-Taylor instability

R. Yan,^{1,2} R. Betti,^{1,2,3} J. Sanz,⁴ H. Aluie,^{1,2} B. Liu,³ and A. Frank³

¹Department of Mechanical Engineering, University of Rochester, Rochester, New York 14627, USA

²Laboratory for Laser Energetics, University of Rochester, Rochester, New York 14627, USA

³Department of Physics and Astronomy, University of Rochester, Rochester, New York 14627, USA

⁴E.T.S.I. Aeronáuticos, Universidad Politécnica de Madrid, Madrid 28040, Spain

(Received 4 November 2015; accepted 7 January 2016; published online 2 February 2016)

The nonlinear evolution of the single-mode ablative Rayleigh-Taylor instability is studied in three dimensions. As the mode wavelength approaches the cutoff of the linear spectrum (short-wavelength modes), it is found that the three-dimensional (3D) terminal bubble velocity greatly exceeds both the two-dimensional (2D) value and the classical 3D bubble velocity. Unlike in 2D, the 3D short-wavelength bubble velocity does not saturate. The growing 3D bubble acceleration is driven by the unbounded accumulation of vorticity inside the bubble. The vorticity is transferred by mass ablation from the Rayleigh-Taylor spikes to the ablated plasma filling the bubble volume. © 2016 AIP Publishing LLC. [<http://dx.doi.org/10.1063/1.4940917>]

I. INTRODUCTION

Inertial confinement fusion (ICF) implosions¹ are unstable to the Rayleigh-Taylor instability (RTI).² The outer surface of an ICF shell is irradiated either by direct laser light or by X ray emitted by a high-Z hohlraum.¹ The radiation absorbed by the shell material causes mass ablation off the shell's outer surface. This rocket effect causes an inward momentum input that leads to the shell's acceleration and compression. It is during this acceleration phase that the outer shell surface is unstable to the RTI, which occurs when a less dense ("lighter") fluid (ablated plasma) pushes on a denser ("heavier") fluid (the unablated plasma). This instability develops into an interchange of heavy with light material. The "bubbles" of lighter fluid rise through the denser fluid, penetrating through the dense shell. This causes the breakup of the shell and/or the injection of ablator material into the central hot plasma (mix). If the integrity of the imploding shell is compromised by the RTI bubbles, the shell is no longer an effective piston and the final compression of the central plasma is greatly reduced. If the hot deuterium-tritium (DT) fuel is mixed with the high-Z ablator material, the enhanced radiation cooling prevents the DT fuel from achieving the thermonuclear ignition conditions. The theory² for the evolution of the classical RTI (without ablation) between two inviscid ideal fluids in a gravitational field has been developed for a sinusoidal perturbation (single mode) in a light fluid with density ρ_l supporting a heavy fluid with density ρ_h separated by a sharp interface. The classical RTI bubbles first grow exponentially in time during the linear phase with a growth rate $\gamma = \sqrt{A_T k g}$, where g is the gravitational acceleration (an effective gravity in the frame of the accelerating shell in ICF), $k = 2\pi/\lambda$ is the perturbation wave number, and A_T is the Atwood number $A_T = (\rho_h - \rho_l)/(\rho_h + \rho_l)$. As the amplitude of the interface perturbation approaches a critical value about equal to 0.1λ , the perturbation amplitude ceases to grow exponentially and the bubbles of light fluid rise at a constant velocity inside the heavy fluid

driven by the buoyancy force against the flow drag. The first nonlinear model introduced by Layzer³ is based on a potential-flow assumption with $A_T \approx 1$. This model describes the RTI growth from the early linear stage to a bubble rising with a constant velocity. Goncharov⁴ extended Layzer's model to include finite density of the light fluid ($A_T \leq 1$) and found an exact solution of the equations describing the fluids near the bubble tip in terms of Fourier series. The asymptotic or terminal bubble velocity U_b^{cl} depends on the dimensionality of the initial perturbation. For 2D and 3D initial perturbations, the terminal bubble velocity is $U_b^{cl2D} = \sqrt{g(1-r_d)/3k}$ and $U_b^{cl3D} = \sqrt{g(1-r_d)/k}$, respectively,⁴ where $r_d = \rho_l/\rho_h$.

Mass ablation at the interface between the two fluids significantly affects the evolution of the RTI (ARTI or ablative Rayleigh-Taylor). In ICF implosions, mass ablation is caused by the laser or by X-ray energy deposited near the shell's surface and used to drive the implosion. It is well known that ablation stabilizes the linear growth in the ARTI⁵⁻⁸ by placing an upper cutoff in k on the unstable spectrum. The penetration velocity of the ablation front into the heavy shell material is called the ablation velocity (V_a) and the linear growth rate of the ARTI can be often approximated using the Takabe's formula⁸ obtained by fitting numerical results

$$\gamma_{ARTI} \approx \alpha \sqrt{kg} - \beta k V_a, \quad (1)$$

where the first term on the right-hand-side is the classical instability drive, and the second term represents the stabilizing effects of ablation. The linear growth rate from the analytic theory^{5,7,9,10} is more complicated than shown in Eq. (1), however, by choosing the coefficient $\beta \approx 2.7$ and $\alpha \approx 0.94$, Eq. (1) represents a fairly accurate fit to the numerical results for a DT ablator.⁷ Different values of α and β have to be chosen for different ablator materials, for example, $\beta \approx 1.7$ and $\alpha \approx 1.0$ for beryllium and CH (plastic) ablators. However, for these two materials, Eq. (1) has to be modified as $\gamma_{ARTI} \approx \alpha \sqrt{kg/(1+kL_m)} - \beta k V_a$ to include the effect of finite density-gradient scale length L_m that is

negligible for DT.⁷ A typical set of direct-drive ignition parameters for DT ablaters yields a cutoff wavelength of less than $10\ \mu\text{m}$ and all modes with wavelengths smaller than the cutoff are linearly stable.⁷

While ablation is stabilizing in the linear regime, the growth of the RTI in the deeply nonlinear regime is accelerated as a result of mass ablation off the fluid interface. An anomalous nonlinear growth, faster than exponential, was observed in the numerical solution of the nonlinear model of Sanz *et al.*¹¹ The nonlinear theory of Ref. 11 treats the vortex flow in the ablated plasma as a small correction to the ablative flow. While this assumption is valid in the linear and weakly nonlinear phases, it does not apply to the deeply nonlinear phase of the bubble evolution. The nonlinear bubbles enclose relatively cold plasma with a large vorticity. Inside the bubble, the vortex flow is greater than the ablative flow and the expansion in Ref. 11 breaks down. Two-dimensional simulations were used in Ref. 12 to study the nonlinear bubble evolution in the deeply nonlinear regime where the vorticity dominates the flow inside the bubbles. The vorticity is originally localized at the fluid interface and transported by mass ablation from the interface into the low density ablated plasma. As the ablated plasma fills the volume within the bubbles, the vorticity accumulates, providing a centrifugal force that acts on the bubble's wall. Similar vorticity accumulation and bubble acceleration phenomena were also reported by Wang *et al.*¹³ In 2D geometry,¹² the bubble acceleration vanishes asymptotically and the bubble's velocity saturates at a value above its classical value U_b^{c2D} . Another numerical study by Igumenshchev *et al.*¹⁴ showed that a small defect on the target surface with a $10\ \mu\text{m}$ radius and $1\ \mu\text{m}$ height drives an RTI bubble that quickly penetrates through the shell. This indicates that even short-wavelength modes can significantly degrade the target performance.

A large body of numerical work exists on the classical (no ablation) 3D RTI. The single-mode problem, as the most fundamental case, has been simulated in both planar^{15–17} and spherical^{17,18} geometry. It was found that the 3D bubbles grow faster than the 2D bubbles in the nonlinearly saturated phase, which is consistent with the difference between U_b^{c2D} and U_b^{c3D} predicted in theory.

The first set of simulations for the 3D ARTI is described in the paper by Dahlburg and Gardner¹⁹ in the early 1990s. They used a laser-absorption model based on inverse bremsstrahlung to induce mass ablation at the surface of a planar foil in the simulations. The initial perturbations are sinusoidal squares. The 3D bubble was observed to grow 10% slower than the 2D bubble but the 3D spike grew 25% faster than the 2D spike. This result appeared at odds with the classical RTI results above indicating faster bubble growth in 3D. Vortex rings were observed generated at the instability interface and ablated off the 3D spike tip due to mass ablation, but the feeding of the vortex rings back into the bubble and the enhancement of bubble growth due to the vortex acceleration mechanism, as presented in Ref. 12, was not observed probably because the mode wavelength was not sufficiently close to the linear cutoff. Later work by Dahlburg *et al.*²⁰ addressed the difference between sinusoidal and Bessel perturbations. It shows that the cylindrical

mode grows faster than the square mode in the nonlinear phase of the bubble growth. Good agreements between simulations and experiments on the ARTI bubble-spike structures were reported in both single-mode²¹ and multi-modes²² regimes. However, the nonlinear evolution of the ARTI bubble in 3D geometry is still an open topic deserving more in-depth study.

In this paper, we study both numerically and analytically the detailed evolution of 3D single-mode ARTI for short-wavelength modes to assess the differences between 3D and 2D bubbles evolution. Like in 2D, we find that 3D bubbles are also accelerated beyond the classical terminal velocity when their wavelengths are close to the linear cutoff. Differently from 2D, saturation of the bubble velocity is not observed in the 3D simulations of single modes near the linear cutoff. This study is focused on single-mode, sinusoidal perturbations in planar foils. Different perturbation shapes other than sinusoidal are not considered here because those are not Fourier modes of the system and require unphysical boundary conditions. The acceleration of the bubble beyond the classical terminal velocity is caused by the accumulation of vorticity inside the bubble driven by mass ablation. This phenomenon only occurs for modes near the cutoff where ablation is important. For mode wavelength much greater than the cutoff wavelength, the effect of ablation-driven bubble acceleration is negligible and the bubble velocity saturates approximately at the classical value. The rest of this paper is organized as follows: In Sec. II, the simulation configurations and results are presented. In Sec. III, a semi-analytical theory is developed to explain the simulation results. In Sec. IV the results are summarized.

II. SIMULATIONS

Our study uses the 3D version of the code *ART3D*.¹² *ART3D* solves the single-fluid hydrodynamic equations including Spitzer thermal conduction²³ over a 3D Cartesian grid. The quasi-equilibrium state from which the ARTI perturbations grow uses profiles typical of direct-drive National Ignition Facility (NIF) targets.²⁴ A planar approximation is valid as long as the target thickness, mode wavelength, and conduction zone region are much smaller than the target radius. This condition is satisfied during most of the

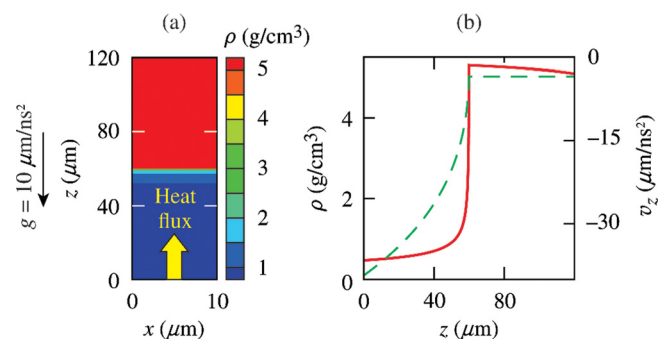


FIG. 1. (a) The simulation setup for the *ART3D* simulation with $\lambda = 10\ \mu\text{m}$. The contour is the initial density distribution. (b) The initial ρ (solid) and v_z (dashed) profiles along the z -axis.

acceleration phase. The simulation setup is shown in Fig. 1. A slab of cold dense DT is placed in the upper half of the simulation box, while the lower half is the ablated plasma with a higher temperature but a lower density. The interface between the dense and the ablated plasma (the ablation front) is kept approximately fixed in space by balancing the ablative pressure with an effective gravity \vec{g} . This is equivalent to solving the fluid equations in the frame of reference of the accelerated foil. The initial gravity is $g_0 = 100 \mu\text{m}/\text{ns}^2$ and the ablation velocity $V_a = 3.5 \mu\text{m}/\text{ns}$, typical of the laser-driven target of Ref. 12. The laser energy flux towards the ablation front is simulated through a constant heat flux assigned at the bottom boundary of the simulation box ($z = 0$). The value of the heat flux corresponding to this ablation rate can be computed through the equilibrium equations. In this case $q = 6.0 \text{ MW}/\mu\text{m}^2$. Since the mass of the foil decreases in time due to ablation, the effective gravity (along the negative z direction) needs to be increased to balance the force from the ablation pressure. This setup offers the advantages of a highly controlled simulation allowing precise evaluations of the bubble penetration velocity into the dense plasma.

Two types of initial perturbations are used in the simulations: 2D perturbations proportional to $\cos(kx) \times \exp(-k|z - z_0|)$ and 3D perturbations proportional to $[\cos(kx) + \cos(ky)] \times \exp(-k|z - z_0|)$, where z_0 is the location of the ablation front. We first consider a perturbation wavelength $\lambda \equiv 2\pi/k = 10 \mu\text{m}$ which is sufficiently close to the linear cut-off for ablation to be important but well into the linearly unstable spectrum ($\lambda > \lambda_{\text{cutoff}} \approx 6 \mu\text{m}$) to grow faster than the mass depleting time due to ablation. For the 2D perturbation, the simulation box is $10 \mu\text{m} \times 120 \mu\text{m}$ with a grid 100×1200 . For the 3D perturbation, the simulation box size is $10 \mu\text{m} \times 10 \mu\text{m} \times 120 \mu\text{m}$ with a grid $100 \times 100 \times 1200$. Periodic boundary conditions are applied on the x - and y -directions and the equilibrium boundary conditions are used on the upper and lower boundaries in the z -direction.

The linear and nonlinear bubble velocities are measured in the simulations. The ARTI bubble velocity (U_b) defined as the speed of the bubble vertex penetrating through the slab of dense fluid is plotted in Fig. 2. The 2D simulations show a bubble growth consistent with the results of Ref. 12. The bubble velocity starts to grow from the value of the ablation

velocity V_a that represents the initial penetration velocity of the ablation front into the heavy fluid. As the bubble amplitude grows, the low-density plasma filling the bubble is colder than the blow-off plasma and the mass ablation off the bubble walls becomes negligible. At this stage, the bubble behaves like in the classical RTI case without ablation and the bubble velocity saturates at the 2D classical value $U_b^{c/2D}$ after about 3 ns. In a later nonlinear stage, the vorticity inside the bubble increases to the point that a large vortex reaches the bubble vertex and accelerates the bubble beyond the classical value $U_b^{c/2D}$. This second bubble acceleration driven by the bubble vorticity raises the bubble velocity to a new saturated value $\sim 1.9U_b^{c/2D}$ [Fig. 2(a)]. The vortex inside the bubble is the result of the accumulation of the vorticity initially located at the ablation front and ablated into the blow-off plasma, and then convected towards the bubble vertex as the ablated plasma fills the bubble volume.

Unlike in 2D, the 3D bubble velocity does not show saturation [Fig. 2(b)]. The classic RTI theory predicts a 3D bubble velocity $U_b^{c/3D}$ that is $\sqrt{3}$ times faster than in 2D. Instead, in the 3D ablative case, the bubble velocity greatly exceeds the classical value $U_b^{c/3D}$ without reaching saturation throughout the simulation period. Such an unbounded growth of the bubble velocity is certainly a concern for inertial fusion implosions. This result was confirmed using a different fluid code *AstroBEAR*.²⁵ The detailed comparison between the two codes will be presented in a future publication.

III. THEORETICAL ANALYSIS AND DISCUSSIONS

To better understand the time evolution of the bubble, we have extended to 3D the Layzer-like^{3,4} model of the bubble-acceleration mechanism due to vortexes of Ref. 12. A well-developed ARTI bubble with the vortexes inside at different stages is shown in Figs. 3(a) and 3(c). The model considers two incompressible fluids ($j = h, l$) of densities ρ_j with a velocity field \mathbf{v}_j satisfying $\nabla \cdot \mathbf{v}_j = 0$. In a frame of reference moving with the unperturbed target, the momentum equation reads as $\rho_j(\partial_t \mathbf{v}_j + \mathbf{v}_j \cdot \nabla \mathbf{v}_j) = -\nabla p_j - \rho_j \mathbf{g}_e$. The interface separating the two fluids $z = z_a(x, y, t)$ is expanded very close to the vertex of the bubble ($x = y = 0$) as $z_a(x, y, t) = a(t) - \alpha(t)x^2 - \beta(t)y^2$, where $a(t)$ is the bubble amplitude and $[2\alpha(t)]^{-1}$, $[2\beta(t)]^{-1}$ are the curvatures along the x - and y -directions. In the surrounding heavy fluid $j = h$, the flow is potential, $\mathbf{v}_h = \nabla \phi_h$ and $\nabla^2 \phi_h = 0$. Under a Layzer type approximation, the potential ϕ_h is written as $\phi_h = \phi_1(t) \exp[-k_y(z - a(t))] \cos(k_y y) + \phi_2(t) \exp[-k_z(z - a(t))] \cos(k_x x)$. For the low density fluid inside the bubble, we assume that the velocity field is given by a potential flow plus a prescribed rotational flow, that is, $\nabla \times \mathbf{v}_l = \boldsymbol{\omega} = -\omega_1 \sin(k_y y) \mathbf{e}_x - \omega_2 \sin(k_x x) \mathbf{e}_y$ and $\mathbf{v}_l = \nabla \phi_l + [k_y^{-1} \omega_1(t) \cos(k_y y) + k_x^{-1} \omega_2(t) \cos(k_x x)] \mathbf{e}_z$. Here ϕ_l also satisfies $\nabla^2 \phi_l = 0$ and is taken as $\phi_l = \mu(t)z + \varphi_1(t) \exp[k_y(z - z_a)] \cos(k_y y) + \varphi_2(t) \exp[k_x(z - z_a)] \cos(k_x x)$. The interface equation is determined from the requirement that surface particles move with the fluid (ablation is neglected at the vertex of the bubble): at z_a we have the kinematic condition $\partial_t z_a + \mathbf{v}_j \cdot \nabla z_a - \mathbf{v}_j \cdot \mathbf{e}_z = 0$. For a given $\omega_1(t)$ and $\omega_2(t)$, these equations are expanded up to $O(x^2)$ and $O(y^2)$, yielding six ordinary differential equations

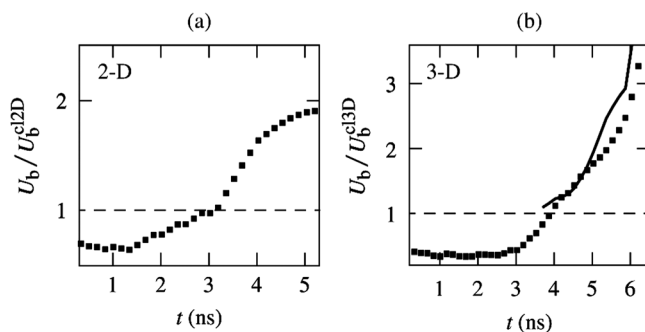


FIG. 2. Ratio of the bubble velocities to the classical values in 2D (a) and 3D (b) simulations for an initial perturbation with $\lambda = 10 \mu\text{m}$. The squares are the simulations and the solid curve is the 3D analytic model of Eq. (3).

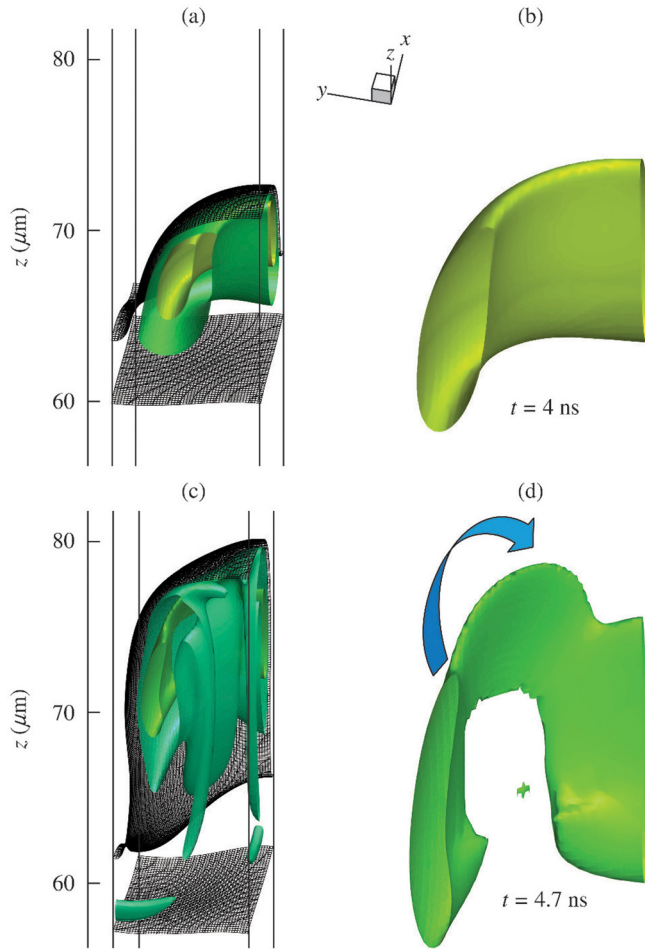


FIG. 3. Iso-surfaces of the azimuthal vorticity $\omega_\phi \equiv \sqrt{\omega_x^2 + \omega_y^2}$ inside a quarter of a bubble in the 3D simulation of $\lambda = 10 \mu\text{m}$ at $t = 4.0 \text{ ns}$ [(a) and (b)] and $t = 4.7 \text{ ns}$ [(c) and (d)]. (a) Outer: $\omega_\phi = 12.5/\text{ns}$; inner: $\omega_\phi = 19/\text{ns}$. (c) Outer: $\omega_\phi = 25/\text{ns}$; inner: $\omega_\phi = 40/\text{ns}$. The inner surfaces of (a) and (c) are zoomed-in in (b) and (d), respectively. The arrow in (d) indicates how the vortex ring gets distorted. Two density iso-surfaces are also plotted as meshes in (a) and (c). Upper mesh: $\rho = 4.5 \text{ g/cm}^3$; lower mesh: $\rho = 1.5 \text{ g/cm}^3$.

(ODEs). Also note that the pressure must be continuous through the interface, $p_h = p_l$. Integrating the momentum equations and expanding up to $O(x^2)$ and $O(y^2)$ terms, the two relevant equations [$O(x^2)$ and $O(y^2)$] are obtained. The set of eight ODEs for the eight unknowns $a(t), \phi_1(t), \phi_2(t), \varphi_1(t), \varphi_2(t), \alpha(t), \beta(t)$, and $\mu(t)$ determines the solution of the problem.

In the case of a square box, namely, $k_y = k_x = k$, $\omega_1(t) = \omega_2(t) = \omega_0(t)$. The symmetry of this configuration leads to $\alpha = \beta$, $\phi_1 = \phi_2$, and $\varphi_1 = \varphi_2$. The final ODE for the 3D bubble velocity v_b is found to be

$$\dot{v}_b = \frac{g(1 - r_d) - kv_b^2 + r_d k^{-1}(\omega_0^2 + 2\dot{\omega}_0)}{1 + r_d}. \quad (2)$$

If a steady vorticity can be reached ($\dot{\omega}_0 = 0$), or $\dot{\omega}_0 \ll \omega_0^2$, a saturated value of v_b can be found as

$$U_b^{rot3D} = \sqrt{\frac{g(1 - r_d)}{k} + r_d \frac{\omega_0^2}{k^2}}, \quad (3)$$

where U_b^{rot3D} is the asymptotic 3D bubble velocity. This is a semi-analytic formula for the bubble velocity with a prescribed ω_0 that can be obtained from the simulation.

Figure 2(b) shows good agreement between the bubble velocities from the simulation and Eq. (3). The simulated bubble velocity (square) grows from the ablation velocity in the linear stage and approaches U_b^{rot3D} (solid line) later in the nonlinear stage. In this comparison, g , r_d , and ω_0 are all from the instantaneous values of the simulation. ω_0 is chosen as the spatial average of the vorticity below the bubble tip

$$\omega_0 = \sqrt{\frac{\int_V \rho(\omega_x^2 + \omega_y^2) dV}{2 \int_V \rho dV}}, \quad (4)$$

where V is the volume inside the bubble and within the length of $1/k$ down from the bubble vertex.

It is the different vortex behavior that causes the lack of saturation of the 3D bubble with respect to 2D. The vortex structure is more complicated in 3D than in 2D. In 2D, a pair of straight vortices are formed perpendicular to the plane of the bubble. In 3D, the vortex is in the shape of a ring inside the bubble. In the early stage, the vortex ring has a regular shape. A quarter of it is shown in Figs. 3(a) and 3(b). The vortex ring evolves into a distorted shape as shown in Figs. 3(c) and 3(d). While a vortex ring is unstable when free in open spaces,²⁶ it is believed that the distortion of the vortex ring in this case is due to the shape distortion of the bubble wall enclosing the vortex. As single-mode bubbles grow, they expand and squeeze each other to form a square-like shape at the bubble waist while maintaining a round shape near the bubble vertex. Since the vortex ring cannot maintain a perfect round shape inside the “square” bubble walls, it becomes warped with the corners of the ring folded toward the bubble vertex [Fig. 3(d)], pushing the center (maxima) of the vortex toward the bubble tip. This increases the vorticity near the bubble tip, hereby enhancing the bubble acceleration. This positive feedback on the bubble acceleration is unique to the 3D geometry and prevents the bubble velocity from reaching a saturated state. Later in time, the behavior of the 3D vortex ring involves twisting and stretching/compressing and the vortex shape can no longer be well characterized by a simple ring.

Shorter-wavelength modes exhibit stronger bubble acceleration. A series of 3D simulations with a wavelength ranging from 7 to 40 μm have been performed to study the bubble acceleration’s dependence on the wavelength. The bubble velocity’s evolution in each case is plotted in Fig. 4 together with the analytic formula U_b^{rot3D} . In general, U_b^{rot3D} predicts reasonably well the asymptotic behavior of the bubble velocity in the nonlinear stage for all of the simulated wavelengths. Good agreement is observed (<10% in bubble velocity) between theory and simulations over most of the bubble evolution. Discrepancies are only significant at later times when the bubble velocities are well above the classical

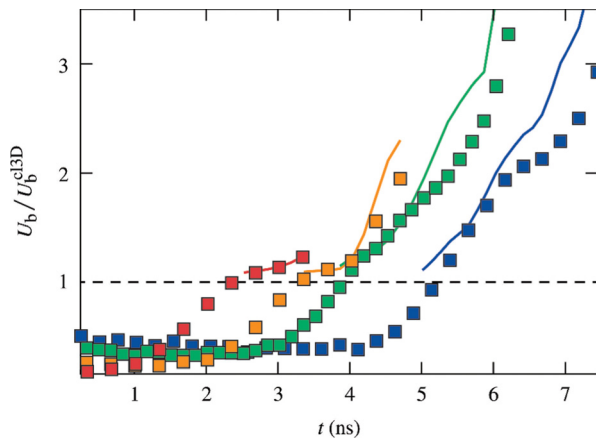


FIG. 4. The bubble velocities from simulations (square) compared with the asymptotic formula U_b^{c3D} (solid line) for $\lambda=40$ (red), 20(orange), 10(green), and 7(blue) μm , respectively.

values and the bubbles have almost penetrated through the entire slab of dense fluid. For the long-wavelength case with $\lambda=40 \mu\text{m}$, the vortex-acceleration effect is weak and the bubble velocity slightly exceeds the classical value. For the shorter wavelengths ($\lambda=7, 10, 20 \mu\text{m}$), the bubble velocity does not achieve saturation during the simulation time. Therefore, terminal bubble velocities of short-wavelength modes can exceed those of longer wavelengths even though their classic bubble velocities U_b^{c3D} are smaller.

As the bubbles of the light fluid penetrate through the heavy fluid, a density plateau inside the bubble is established. The density inside the bubble depends on the mode wavelength. The value of density inside the bubble is approximately constant as the bubble grows deeply into the nonlinear phase. Determining the bubble density is important to assessing the amount of material from the cold fuel and/or from the outer ablator that is injected inside the hot central DT plasma in an inertial fusion implosion. The main consequence of this material-mixing process is the reduction of the fusion reactivity in the central plasma. Figure 5 shows that the bubble density increases at shorter wavelengths, indicating that short-wavelength modes can be effective in driving mix in ICF.

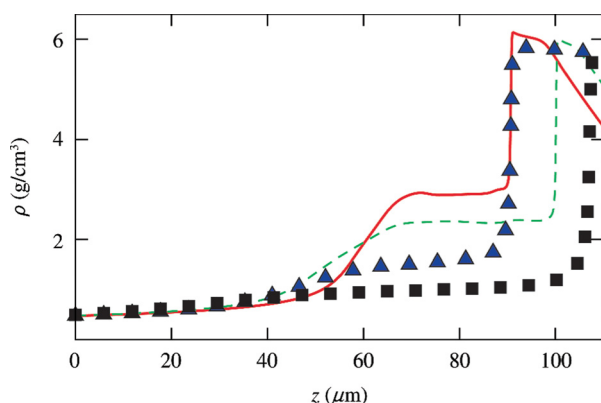


FIG. 5. The density profiles along the bubble axes. Solid: $\lambda=7 \mu\text{m}$ at $t=6.8 \text{ ns}$; dashed: $\lambda=10 \mu\text{m}$ at $t=5.7 \text{ ns}$; delta: $\lambda=20 \mu\text{m}$ at $t=4.2 \text{ ns}$; square: $\lambda=40 \mu\text{m}$ at $t=4.2 \text{ ns}$. Shorter wavelength bubbles are denser.

IV. SUMMARY

To summarize, a fluid code *ART3D* has been developed and used to study the nonlinear evolution of the ablative Rayleigh-Taylor instability in three dimensions. As the mode wavelength approaches the cutoff of the linear spectrum (short wavelength modes), it is found that the 3D terminal bubble velocity greatly exceeds both the 2D value and the classical 3D bubble velocity. Unlike in 2D, the 3D short-wavelength bubble velocity does not saturate. A Layzer-like model has been developed and can quantitatively explain the 3D bubble acceleration driven by the unbounded accumulation of vorticity inside the bubble. The vorticity's build-up inside the bubble is caused by mass ablation. Mass ablation convects the vorticity generated by the Rayleigh-Taylor instability of the ablation front into the low-density ablated plasma. As the ablated plasma flows into the bubble, it carries its vorticity inside the bubble and produces a strong vortex near the bubble tip. The centrifugal force of this vortex drives the bubble acceleration beyond the classical terminal velocity. The simulations indicate that the density inside the bubble is larger at shorter wavelengths, implying that short-wavelength modes are more effective in driving mix than long wavelength modes.

ACKNOWLEDGMENTS

This work was supported by the Office of Fusion Energy Sciences Nos. DE-FG02-04ER54789, DE-SC0014318, the Department of Energy National Nuclear Security Administration under Award No. DE-NA0001944, the Ministerio de Ciencia e Innovación of Spain (Grant No. ENE2011-28489), the University of Rochester, the New York State Energy Research and Development Authority, and the LANL LDRD program through project number 20150568ER. The support of the U.S. DOE does not constitute an endorsement by that agency of the views expressed in this paper.

- ¹J. D. Lindl, *Inertial Confinement Fusion* (Springer, New York, 1998).
- ²L. Rayleigh, *Scientific Papers II* (Cambridge University Press, Cambridge, England, 1900), p. 200.
- ³D. Layzer, *Astrophys. J.* **122**, 1 (1955).
- ⁴V. N. Goncharov, *Phys. Rev. Lett.* **88**, 134502 (2002).
- ⁵J. Sanz, *Phys. Rev. Lett.* **73**, 2700 (1994).
- ⁶R. Betti, V. N. Goncharov, R. L. McCrory, P. Sorotokin, and C. P. Verdon, *Phys. Plasmas* **3**, 2122 (1996).
- ⁷R. Betti, V. N. Goncharov, R. L. McCrory, and C. P. Verdon, *Phys. Plasmas* **5**, 1446 (1998).
- ⁸H. Takabe, K. Mima, L. Montierth, and R. Morse, *Phys. Fluids* **28**, 3676 (1985).
- ⁹V. N. Goncharov, R. Betti, R. L. McCrory, P. Sorotokin, and C. P. Verdon, *Phys. Plasmas* **3**, 1402 (1996).
- ¹⁰A. R. Piriz, J. Sanz, and L. F. Ibanez, *Phys. Plasmas* **4**, 1117 (1997).
- ¹¹J. Sanz, R. Betti, R. Ramis, and J. Ramirez, *Plasma Phys. Controlled Fusion* **46**, B367 (2004).
- ¹²R. Betti and J. Sanz, *Phys. Rev. Lett.* **97**, 205002 (2006).
- ¹³L. F. Wang, W. H. Ye, X. T. He, W. Y. Zhang, Z. M. Sheng, and M. Y. Yu, *Phys. Plasmas* **19**, 100701 (2012).
- ¹⁴I. V. Igumenshchev, V. N. Goncharov, W. T. Shmayda, D. R. Harding, T. C. Sangster, and D. D. Meyerhofer, *Phys. Plasmas* **20**, 082703 (2013).
- ¹⁵G. Tryggvason and S. O. Unverdi, *Phys. Fluids A* **2**, 656 (1990).
- ¹⁶T. Yabe, H. Hoshino, and T. Tsuchiya, *Phys. Rev. A* **44**, 2756 (1991).

- ¹⁷J. Hecht, D. Ofer, U. Alon, D. Shvarts, S. Orszag, and R. McCrory, *Laser Part. Beams* **13**, 423 (1995).
- ¹⁸H. Sakagami and K. Nishihara, *Phys. Rev. Lett.* **65**, 432 (1990).
- ¹⁹J. P. Dahlburg and J. H. Gardner, *Phys. Rev. A* **41**, 5695 (1990).
- ²⁰J. P. Dahlburg, J. H. Gardner, G. D. Doolen, and S. W. Haan, *Phys. Fluids B* **5**, 571 (1993).
- ²¹M. M. Marinak, B. A. Remington, S. V. Weber, R. E. Tipton, S. W. Haan, K. S. Budil, O. L. Landen, J. D. Kilkenny, and R. Wallace, *Phys. Rev. Lett.* **75**, 3677 (1995).
- ²²M. M. Marinak, S. G. Glendinning, R. J. Wallace, B. A. Remington, K. S. Budil, S. W. Haan, R. E. Tipton, and J. D. Kilkenny, *Phys. Rev. Lett.* **80**, 4426 (1998).
- ²³L. Spitzer and R. Härm, *Phys. Rev.* **89**, 977 (1953).
- ²⁴P. W. McKenty, V. N. Goncharov, R. P. J. Town, S. Skupsky, R. Betti, and R. L. McCrory, *Phys. Plasmas* **8**, 2315 (2001).
- ²⁵A. J. Cunningham, A. Frank, P. Varnire, S. Mitran, and T. W. Jones, *Astrophys. J., Suppl. Ser.* **182**, 519 (2009).
- ²⁶S. E. Widnall and J. P. Sullivan, *Proc. R. Soc. A* **332**, 335 (1973).